*metals*

MDPI

*Communication*

# $MoSe_2$ Complex with N and B Dual-Doped 3D Carbon Nanofibers for Sodium Batteries

**Weigang Zhao, Cuirong Liu * and Xu Yin**

College of Materials Science and Engineering, Taiyuan University of Science and Technology, Taiyuan 030024, China
* Correspondence: tyust77@126.com

**Abstract:** The sodium battery is one of the best energy storage technologies due to its abundant resource reserves and excellent energy storage ability. As a two-dimensional layered transition metal, molybdenum selenide ($MoSe_2$) has large interlayer spacing and a high theoretical capacity (470 $mAh{\cdot}g^{-1}$). Its structure is suitable for the negative electrode of sodium-ion batteries, with a large ionic radius and slow ion diffusion kinetics. However, it is difficult for the rate capability and cycling performance of $MoSe_2$ to meet practical needs due to a weak intrinsic electron transport ability and volume expansion during sodium absorption. The hydrothermal synthesis method was used to synthesize the $MoSe_2$ complex based on boron and nitrogen dual-doped 3D carbon fibers obtained from bacterial cellulose membranes ($MoSe_2$/N&B-BCM) for sodium batteries. Additionally, electrochemical analysis and experimental characterization were performed. In summary, the experimental analysis shows that $MoSe_2$/N&B-BCM has excellent conductivity, structural integrity, cyclability (328 $mAh{\cdot}g^{-1}$ after 100 cycles at a 0.5 c constant rate), and rate stability.

**Keywords:** N and B dual-doped; 3D interconnected carbon fibers; $MoSe_2$ complexed

check for updates

**Citation:** Zhao, W.; Liu, C.; Yin, X. $MoSe_2$ Complex with N and B Dual-Doped 3D Carbon Nanofibers for Sodium Batteries. *Metals* **2023**, *13*, 518. https://doi.org/10.3390/met13030518

Academic Editors: Jürgen Eckert and Claudio Pistidda

Received: 29 January 2023
Revised: 27 February 2023
Accepted: 1 March 2023
Published: 3 March 2023



## 1. Introduction

With the massive consumption of fossil resources, the importance of new energy sources is becoming more and more prominent. In recent years, high specific energy, no memory effect, safety, long cycle life, and high efficiency have become part of the features of energy storage used in different devices, such as cell phones, laptops, and electric vehicles [1–3]. As one of the most widely used new energy sources, lithium-ion batteries are widely used in human daily life [4,5]. However, the very limited reserves of lithium on earth and their uneven distribution have limited the development of lithium-ion batteries in China. Therefore, the search for new low-cost and resource-rich high-performance secondary battery systems to replace lithium-ion batteries has become the key to sustainable energy development. Sodium-based energy storage systems have shown high promise due to their abundant sodium sources, low cost, and wide availability. Therefore, sodium-ion batteries have become one of the most promising directions for the future development of energy storage batteries [6–8].

However, the main obstacle to the development of sodium-ion batteries is the large radius of $Na^+$, as this results in slow reaction kinetics. This limits the practical applications of sodium batteries [9] due to the large radius of $Na^+$ (0.102 nm) (compared with 0.076 nm for $Li^+$) and a large diffusion potential barrier. Therefore, novel sodium storage materials are urgently required, and the development of high-capacity, long-cycle-life anode materials is particularly critical. In recent years, carbon materials, alloy materials, and metal–oxygen/sulfur/selenide have been widely used (Figure 1), of which carbon materials have a stable cycling performance but low capacity [10]; alloys have a high theoretical capacity but huge volume expansion [11]; and metal oxides have a high theoretical capacity but low electrical conductivity [12]. The ideal anode material for sodium-ion batteries

needs to meet the requirements of excellent conductivity, small volume expansion, and long cycle life.

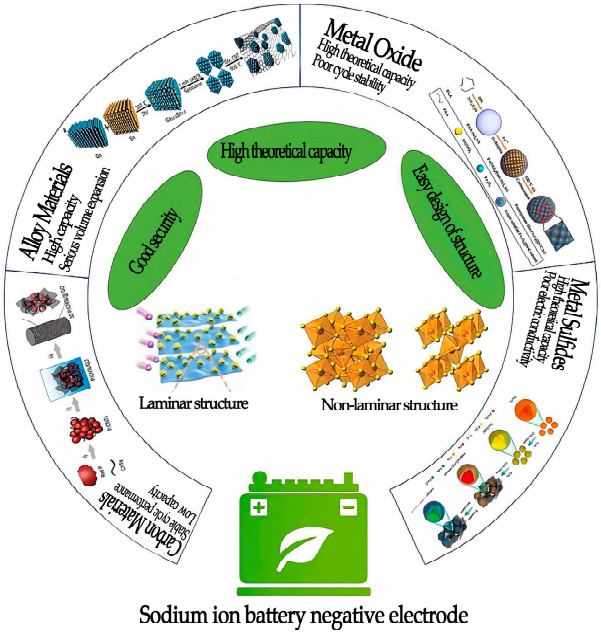


**Figure 1.** Anode materials for sodium-ion batteries (color online).

$MoSe_2$ has a sandwich structure bonded between in-plane atoms and coupled with weak vertical van der Waals forces. It is beneficial for the intercalation/deintercalation of Na ions. It has been widely studied as an anode material for sodium-ion batteries due to its high theoretical capacity (470 m Ah $g^{-1}$) and large layer spacing (0.646 nm). $MoSe_2$ has many attractive features, including low cost, high quantity, environmental friendliness, and stable rate performance. Therefore, it is considered to be the most promising anode material for sodium-ion batteries. Despite so many advantages, there is still considerable room for improving the performance of $MoSe_2$ anode materials before practical applications, which are mainly limited by the limited-contact active sites of sodium ions and long ion diffusion paths [13]. Moreover, repeated $Na^+$ embedding and de-embedding during long-term cycling causes significant mechanical stress and volume changes in $MoSe_2$, which may cause $MoSe_2$ accumulation and aggregation, leading to poor cycling stability [14]. To solve these problems, various strategies have been developed to improve the electrical conductivity and structural stability of $MoSe_2$, such as the optimization of particle size or morphology and the fabrication of $MoSe_2$/carbon hybrids [15–20].

In the past few decades, $MoSe_2$ complexes with carbon ($MoSe_2$/C, $MoSe_2$/BCM, and $MoSe_2$@N,P-C) have produced good electronic results. Therefore, a $MoSe_2$ complex with carbon is a good choice for energy storage devices. Liu et al. synthesized sheet-like $MoSe_2$/C composites [21]. After 50 cycles, the reversible specific capacity is 576.7 mAh·$g^{-1}$ at a current density of 100 mA·$g^{-1}$. Zhang et al. successfully synthesized 3D core–sheath-structured carbon nanofiber@nitrogen-doped porous carbon for sodium-ion batteries (SIBs) [22]. It shows an outstanding electrochemical performance, including a high reversible specific capacity (240 mAh·$g^{-1}$ at 100 mA·$g^{-1}$ over 100 cycles), an excellent rate performance (146.5 mAh·$g^{-1}$ at 1000 mA·$g^{-1}$), and superior cycling stability (148.8 mAh·$g^{-1}$ at 500 mA·$g^{-1}$ over 400 cycles). Dual nitrogen and boron elements on a bacterial cellulose membrane (BCM) significantly improve both the cathode and anode performance of sodium-ion batteries, thus alleviating the mismatch between the two electrodes [23].

Herein, to improve the cycle performance of $MoSe_2$, we design and synthesize a novel $MoSe_2$ complex with boron and nitrogen dual-doped 3D carbon nanofibers ($MoSe_2$/N&B-

BCM) for sodium batteries by using the hydrothermal synthesis method. $MoSe_2$/N&B-BCM was compared with $MoSe_2$/BCM, N&B-BCM, and BCM to identify the better electronic performance. After optimization, $MoSe_2$/N&B-BCM exhibits excellent cyclability (328 $mAh \cdot g^{-1}$ after 100 cycles at a 0.5 $A \cdot g^{-1}$ current density) and good rate performance. These outstanding electrochemical performances should be associated with the novel 3D architecture, in which the N and B elements are mainly homogeneously dispersed on the fibers of the BCM. $MoSe_2$ complexed with N- and B-doped BCM produced stable composites due to the dual doping with N and B elements; its electronic point actives were also improved, resulting in an excellent rate and stability.

## 2. Experimental Section

### *2.1. Reagents and Instruments*

Se, 99.9% by mass; hydrazine hydrate, 98.5% by mass; ammonium borate tetrahydrate, 98.3% by mass; sodium molybdate dihydrate, 99.5% by mass; and polyvinylidene fluoride (PVDF), battery grade, were obtained from Shanghai Aladdin Biochemical Technology Co., Ltd. (Shanghai, China). NaClO4, 1.0 mol/L; ethylene carbonate (EC); and diethyl carbonate (DC) were obtained from China National Chemical Engineering Co., Ltd. (Beijing, China). Anhydrous ethanol, 99.7% mass fraction, was obtained from Yantai Far East Fine Chemical Co., Ltd. (Yantai, China) and bacterial cellulose membrane from Guilin Qihong Technology Co., Ltd. (Guilin, China).

Glove box: SG1200/750TS, Michelona (China) Co., Ltd (Shanghai, China). Ultrasonic cleaner: KQ5200DE, Kunshan Ultrasonic Instruments Co., Ltd. (Suzhou, China). Magnetic mixer: DF-101S, Gongyi Yuhua Instrument Co., Ltd. (Zhengzhou, China). Blast drying oven: GZX-9076 MBE, Shanghai Boxun Industrial Co., Ltd. (Shanghai, China). Tube furnace: MFLGKD405-12, Shanghai Muffle Furnace Technology Instruments Co., Ltd. (Shanghai, China). Electrochemical workstation: CHI660E, Shanghai Chenhua Instruments Co., Ltd. (Shanghai, China). Battery testing system: CT2001A, Wuhan Blue Electric Electronic Co., Ltd. (Wuhan, China). Three mouth flasks, beakers, vacuum pumps, pipettes, etc.: Beijing Xinville Glass Instruments Co., Ltd. (Beijing, China). Electronic balance: FA2004N, Shanghai Jinghai Instrument Co., Ltd. (Shanghai, China). Tablet press: 50T press, Jiaxing Tongli Hardware Machinery Co., Ltd. (Jiaxing, China).

X-ray diffractometer (XRD): D8 Advance, Bruker, Germany. Confocal laser micro spectrometer (Raman): InviaQontor, Renishaw, London, UK. Transmission electron microscope (TEM): JEM-2100F, JEOL, Tokio, Japan. Scanning electron microscope (SEM): LYRA 3 XMH, TESCAN, Brno, Czech Republic. Energy spectrometer (EDS): X-MaxN 80T IE250, Oxford, UK. X-ray Photoelectron Spectrometer (XPS): AXIS Supra, Kratos Analytical Ltd., Manchester, UK. LAND battery programmable tester: CT2001A, Wuhan Blue Electric Electronics Co., Wuhan, China.

### *2.2. Materials Syntheses*

#### 2.2.1. Preparation of BCM

First, the bacterial cellulose membrane (BCM) was cut into species (40 × 60 mm) and washed several times with deionized water, and the prepared BCM was immersed in 100 mL of DI water for 24 h, slowly stirred at room temperature, and then freeze-dried for 24 h. The freeze-dried product was placed in a tube furnace and sintered in nitrogen at 600 °C for 3 h. After carbonization, the product was thoroughly washed in hot deionized water and dried overnight at 80 °C.

#### 2.2.2. Preparation of $MoSe_2$/BCM

First, the BCM was stirred to break it up. An amount of 158 mg of selenium powder was dissolved in 5 mL of hydrazine, as solution A, and then 242 mg of sodium molybdate was dissolved in a mixture of ethanol–water (ethanol:water, 1:1). The loading volume of the reaction solution (a combination of ethanol and water) was 50%, as solution B. Moreover, solution A was stirred with the BCM and then slowly added to solution B. The resulting

mixed liquid was sealed in a reaction vessel and reacted at 180 °C for 10 h. The resulting membrane was washed with deionized water and ethanol, and then freeze-dried for 24 h. The freeze-dried product was placed in a tube furnace and sintered in nitrogen at 350 °C for 1 h and then heated to 800 °C for another 1 h. After carbonization, the product was thoroughly washed in hot deionized water and dried overnight at 80 °C.

#### 2.2.3. Preparation of N&B-BCM

First, after cutting the BCM into species (40 × 60 mm) and washing several times with deionized water, the prepared BCM was immersed in 100 mL of a 0.1 M $NH_4HB_4O_7$ aqueous solution for 24 h, slowly stirred at room temperature, and then freeze-dried for 24 h. Then, the freeze-dried product was placed in a tube furnace and sintered in nitrogen at 600 °C for 3 h. After carbonization, the product was thoroughly washed in hot deionized water and dried overnight at 80 °C.

#### 2.2.4. Preparation of $MoSe_2$/N&B-BCM

First, after cutting N&B-BCM into species (40 × 60 mm) and washing several times with deionized water, the prepared BCM was immersed in 100 mL of a 0.1 M $NH_4HB_4O_7$ aqueous solution for 24 h, slowly stirred at room temperature, and then freeze-dried for 24 h. Then, the freeze-dried product was placed in a tube furnace and sintered in nitrogen at 600 °C for 3 h. After carbonization, the product was thoroughly washed in hot deionized water and dehydrated overnight at 80 °C.

Then, the N&B-BCM was stirred to break it. An amount of 158 mg of selenium powder was dissolved in 5 mL of hydrazine, as solution A, and then 242 mg of sodium molybdate was dissolved in a mixture of ethanol–water (ethanol:water, 1:1). The loading volume of the reaction solution (a combination of ethanol and water) was 50%, as solution B. Moreover, solution A was stirred with N&B-BCM and then slowly added to solution B. The resulting mixed liquid was sealed in a reaction vessel and reacted at 180 °C for 10 h. The resulting membrane was washed with deionized water and ethanol, and then freeze-dried for 24 h. The freeze-dried product was placed in a tube furnace and sintered in nitrogen at 350 °C for 1 h and then heated to 800 °C for another 1 h. After carbonization, the product was thoroughly washed in hot deionized water and dried overnight at 80 °C.

### *2.3. Electrochemical Measurements*

Preparation of electrodes:

(1) The slurry preparation: The active material (the composite material detailed above), conductive material (acetylene black), and binder (the solute was PVDF, the solvent was NMP, and the mass fraction was 8 wt%) were weighed. The active material and the conductive material were ground in an agate mortar for 40 min, and then the mixed powder was poured into a 5 mL glass bottle with a cover. The binder was added and then stirred at a constant speed for 3 h.

(2) The electrode preparation: A 10 × 15 cm piece of copper foil was wiped with an alcohol cotton ball to remove surface dust; the evenly stirred slurry was coated onto the surface of the copper foil; the foil was kept in a vacuum drying oven for 12 h, and the temperature was set at 80 °C; the dried copper foil was further impacted with a punch to obtain an electrode sheet with a diameter of 14 mm; the obtained electrode sheet was placed in a tablet press with a 10 MPa pressure and was pressed down and kept as such for 3 s; and the quality of the electrode sheet was weighed. A card machine was used to make the active material copper foil into several Ø = 14 mm copper foils, and they were weighed, and the average mass of the Ø = 14 mm copper foils was calculated. Combining the average mass of the electrode sheet and copper foil of Ø = 14 mm with the slurry ratio, the mass of the active material on the surface of the electrode sheet was calculated. The weight of the electrode was 2 mg/cm$^2$.

(3) The battery assembly: The entire battery assembly process was carried out in a vacuum glove box filled with Ar. All the batteries used in this paper were CR2025

button cells. From bottom to top, they have a positive electrode shell, an electrode sheet (the side coated with the active material facing up), a separator, a sodium metal sheet, nickel foam, and a negative electrode shell. Two~three drops of electrolyte were added. After assembly was complete, a paper towel was used to wipe off the excess electrolyte that spilled out of the battery to prevent the battery from short-circuiting.

## 3. Results and Discussion

The phase structure of the samples was investigated using X-ray powder diffraction (XRD). Figure 2 shows the XRD patterns of $MoSe_2$/N&B-BCM, $MoSe_2$/BCM, N&B-BCM, and BCM. Compared with pure BCM, N&B-BCM, $MoSe_2$/N&B-BCM, and $MoSe_2$/BCM show 3 peaks at around 30°, 38°, and 55°, respectively. These correspond to the (100), (103), and (110) planes and suggest that N and B dual-doped BCM carbonates materials. Except for the carbon peaks, $MoSe_2$ (JCPDF 29-0914) is easily located from the 13.60°, 32.10°, 38.32°, 47.29°, and 56.98° diffraction peaks. It is shown that $MoSe_2$ grew well on the BCM and N&B-BCM. There are 2 peaks corresponding to the (100) and (110) peaks of MoSe2. A total of 2 obvious peaks appear at 2θ = 13.7°, 37.9°, which correspond to the (002) and (103) planes, suggesting that the (002) and (103) interlayer spacing of the freshly prepared $MoSe_2$ was dramatically changed. After the N-B doping treatment, the diffraction peaks become much sharper with increased intensity, indicating improved crystallinity. Besides the 2 (100) and (110) diffraction peaks, 2 additional peaks at 13.7 and 37.9° are observed, which can be correlated with the (002) and (103) diffraction peaks of $MoSe_2$ (JCPDF 29-0914).

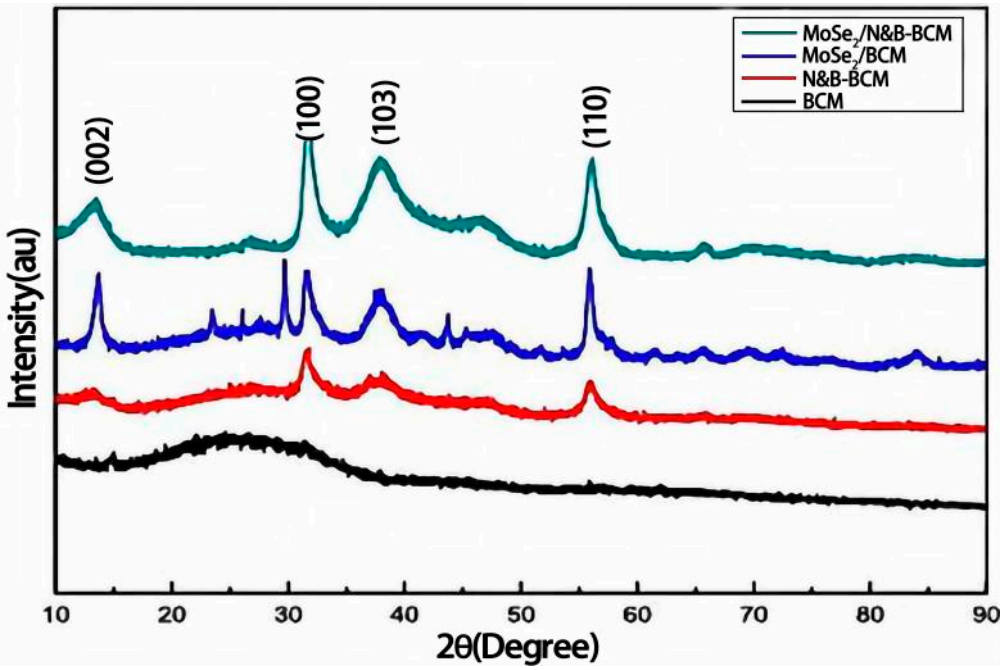


**Figure 2.** XRD patterns of $MoSe_2$/N&B-BCM, $MoSe_2$/BCM, N&B-BCM, and BCM.

To analyze the chemical composition on the surface and the valence of states in the sheet-like $MoSe_2$/N&B-BCM composites, X-ray photoelectron spectroscopy (XPS) measurements were carried out in the region of $MoSe_2$/N&B-BCM. The survey spectrum of the composites (Figure 3a) further shows the C1s spectrum, which could be deconvoluted into one peak. The sharp peak at around 284.6 eV corresponds to sp2-C with C=C bonds. As shown in Figure 3b, the N1s spectrum can be deconvolved into 2 peaks, which can be assigned to pyridinic N at 395.8 eV and quaternary N at 402.1 eV. The high-resolution Mo3d spectrum of the composites exhibits 2 peaks at 229 eV and 232.1 eV (Figure 3c), corresponding to the Mo3d5/2 and 3d3/2 spin-orbit peaks of MoSe2, confirming the existence of the Mo IV state. The 3d height of the Se element is split into 2 well-defined

peaks at 54.5 eV and 55.4 eV (Figure 3d), corresponding to the Se3d5/2 and Se3d3/2 characterized peaks, further illustrating the products are $MoSe_2$/N&B-BCM [24–27].

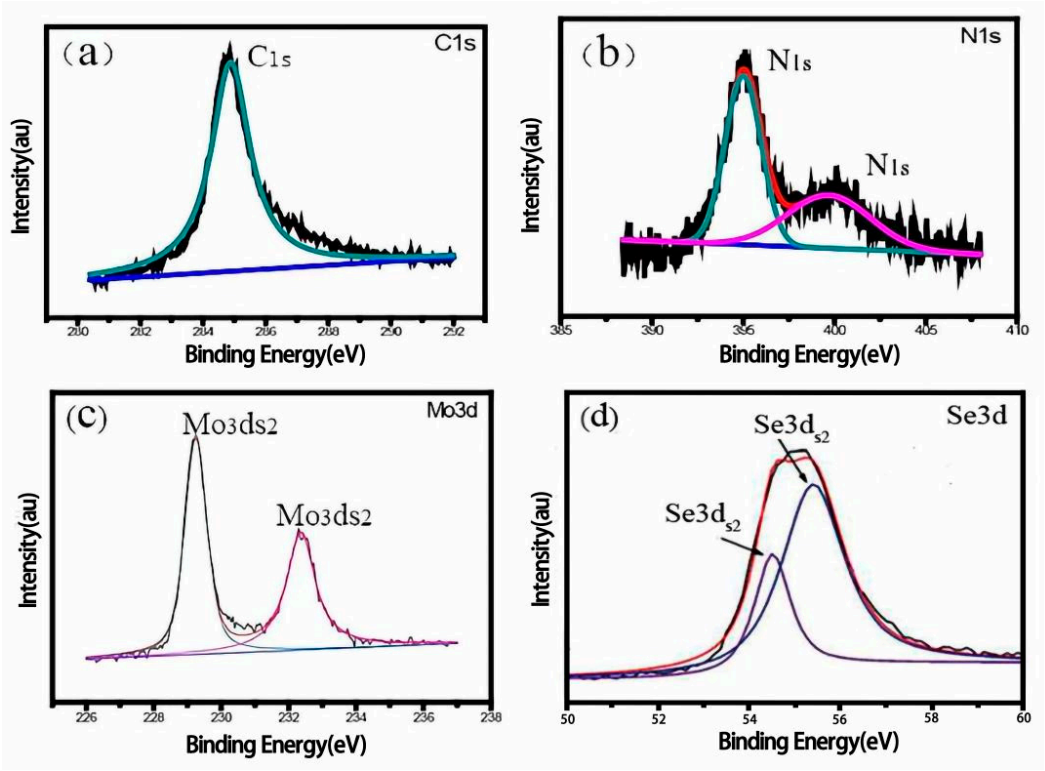


**Figure 3.** (**a**) The XPS C 1s spectrum of $MoSe_2$/N&B-BCM, (**b**) the XPS N 1s spectrum of $MoSe_2$/N&B-BCM, (**c**) the XPS Mo 3d spectrum of $MoSe_2$/N&B-BCM, and (**d**) the XPS Se 3d spectrum of $MoSe_2$/N&B-BCM.

The morphologies of all the samples were investigated using scanning electron microscopy (SEM). When BCM was doped with N and B (Figure 4c), it exhibited an interconnected fiber morphology with a diameter of 1 um. When was complexed with $MoSe_2$ (Figure 4d), it showed a nanoflower structure, confirming that $MoSe_2$ had already grown on the carbon fibers. Figure 4e,f shows the $MoSe_2$/N&B-BCM system, which exhibits a stable structure like a rice spike. The elemental mapping images of $MoSe_2$/N&B-BCM in Figure 4g display that the Mo, Se, C, N, and B elements are evenly distributed (Figure 4h–l). In the synthesis of $MoSe_2$/N&B-BCM, hydrazine hydrate and ethylenediamine (EDA) were used, so the N and B elements were present in the composite. The EDS spectra further confirm the existence of Mo, Se, C, N, and B.

Figure 5a indicates that $MoSe_2$/N&B-BCM exhibits an outstanding electrochemical performance as an anode. $MoSe_2$/N&B-BCM has the highest capacity of 328 $mAh{\cdot}g^{-1}$ at 0.5 $A{\cdot}g^{-1}$. According to Figure 5b, $MoSe_2$/N&B-BCM has excellent cyclability when compared with BCM, N&B-BCM, and $MoSe_2$/BCM as an anode, and $MoSe_2$/N&B-BCM exhibits the highest capability at 328 $mAh{\cdot}g^{-1}$ at 0.5 $A{\cdot}g^{-1}$. $MoSe_2$/N&B-BCM had a stable rate performance at 328 $mAh{\cdot}g^{-1}$, 260 $mAh{\cdot}g^{-1}$, 202 $mAh{\cdot}g^{-1}$, 153 $mAh{\cdot}g^{-1}$, 121 $mAh{\cdot}g^{-1}$, 205 $mAh{\cdot}g^{-1}$, 246 $mAh{\cdot}g^{-1}$, and 309 $mAh{\cdot}g^{-1}$, at a 0.1 $A{\cdot}g^{-1}$, 0.2 $A{\cdot}g^{-1}$, 0.5 $A{\cdot}g^{-1}$, 1 $A{\cdot}g^{-1}$, 2 $A{\cdot}g^{-1}$, 0.5 $A{\cdot}g^{-1}$, 0.2 $A{\cdot}g^{-1}$, and 0.1 $A{\cdot}g^{-1}$ current density (Figure 5c). Figure 5d shows the charge–discharge curve of the $MoSe_2$/N&B-BCM electrode at a magnification of 0.1 $A{\cdot}g^{-1}$. The composite anode has a satisfactory initial discharge and charge capacity of 480 $mAh{\cdot}g^{-1}$ and 328 $mAh{\cdot}g^{-1}$, respectively, with a coulombic efficiency of 68.3%. The SEI film provides such an irreversible capacity. In the following two cycles, both curves coincide very well, implying stable SEI film formation and high electrochemical reversibility [28].

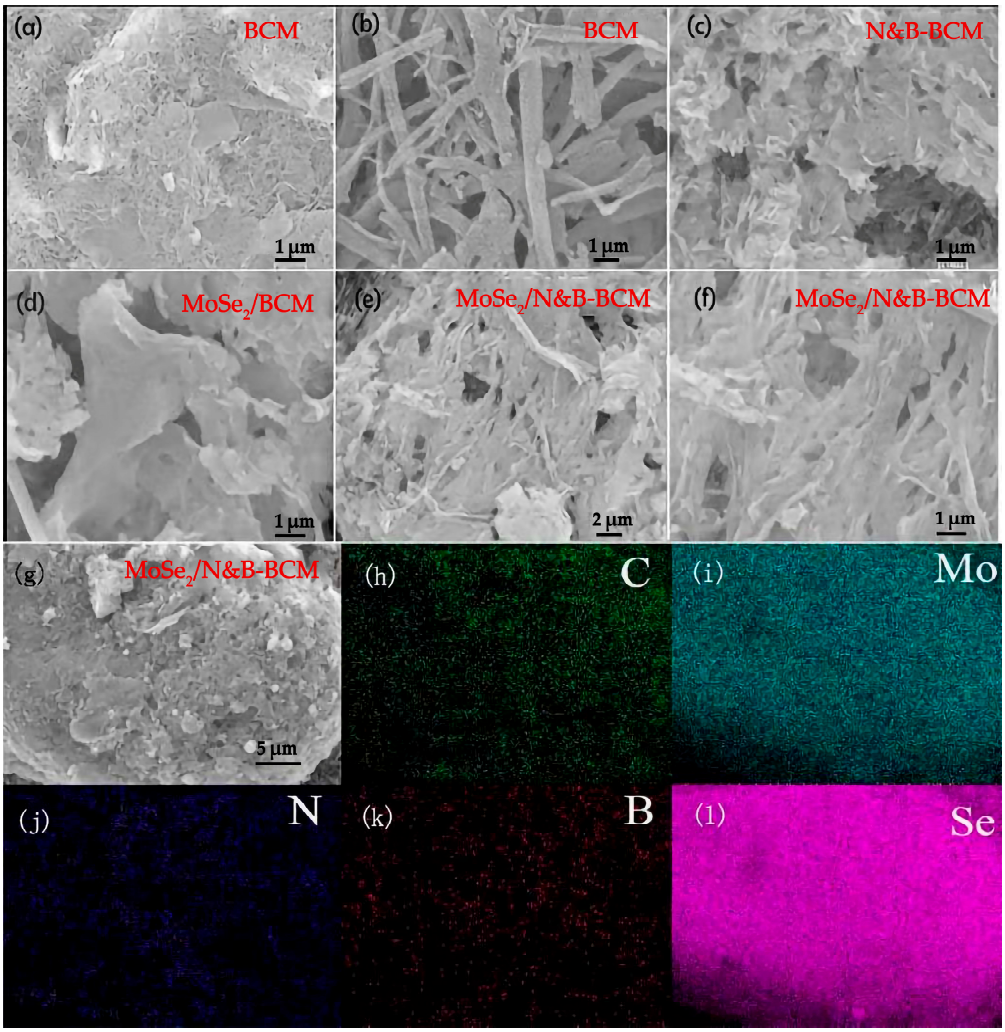


**Figure 4.** The SEM images of BCM (**a**,**b**); N&B-BCM (**c**); $MoSe_2$/ BCM (**d**); and $MoSe_2$/N&B-BCM (**e**–**g**). The EDS images of $MoSe_2$/N&B-BCM (**h**–**l**).

The initial 4 cycles of the current voltage curves of $MoSe_2$/N&B-BCM in the range 0.01 V–3 V (vs. $Na^+/Na$) at a scan rate of 0.1 $mV \cdot s^{-1}$ are presented in Figure 5e, which are different from those of BCM, N&B-BCM, and $MoSe_2$/BCM. An irreversible cathodic peak was observed for the $MoSe_2$/N&B-BCM electrode at 1.08 V in the first cycle but disappeared in the subsequent processes, showing a typical behavior of a solid electrolyte interface (SEI) [29]. In sharp contrast, a pair of redox peaks at 1.85 and 1.10 V were observed in all CV curves of $MoSe_2$/N&B-BCM, which are attributed to the redox reactions between Mo and $Na^+$ [30]. Moreover, the CV curves of the second, third, and fourth cycles were nearly identical, suggesting the excellent cycling stability of the $MoSe_2$/N&B-BCM electrode.

As shown in Figure 5f and Table 1, we tested the BCM, N&B-BCM, $MoSe_2$/BCM, and $MoSe_2$/N&B-BCM sodium batteries' EIS in order to understand the superior reaction dynamics of the $MoSe_2$/N&B-BCM electrode. The semicircle in the medium-frequency region in the Nyquist plots typically indicates the electrochemical reaction impedance. In contrast, the sloping line in the low-frequency region corresponds to $Na^+$ diffusion in the electrodes [31].

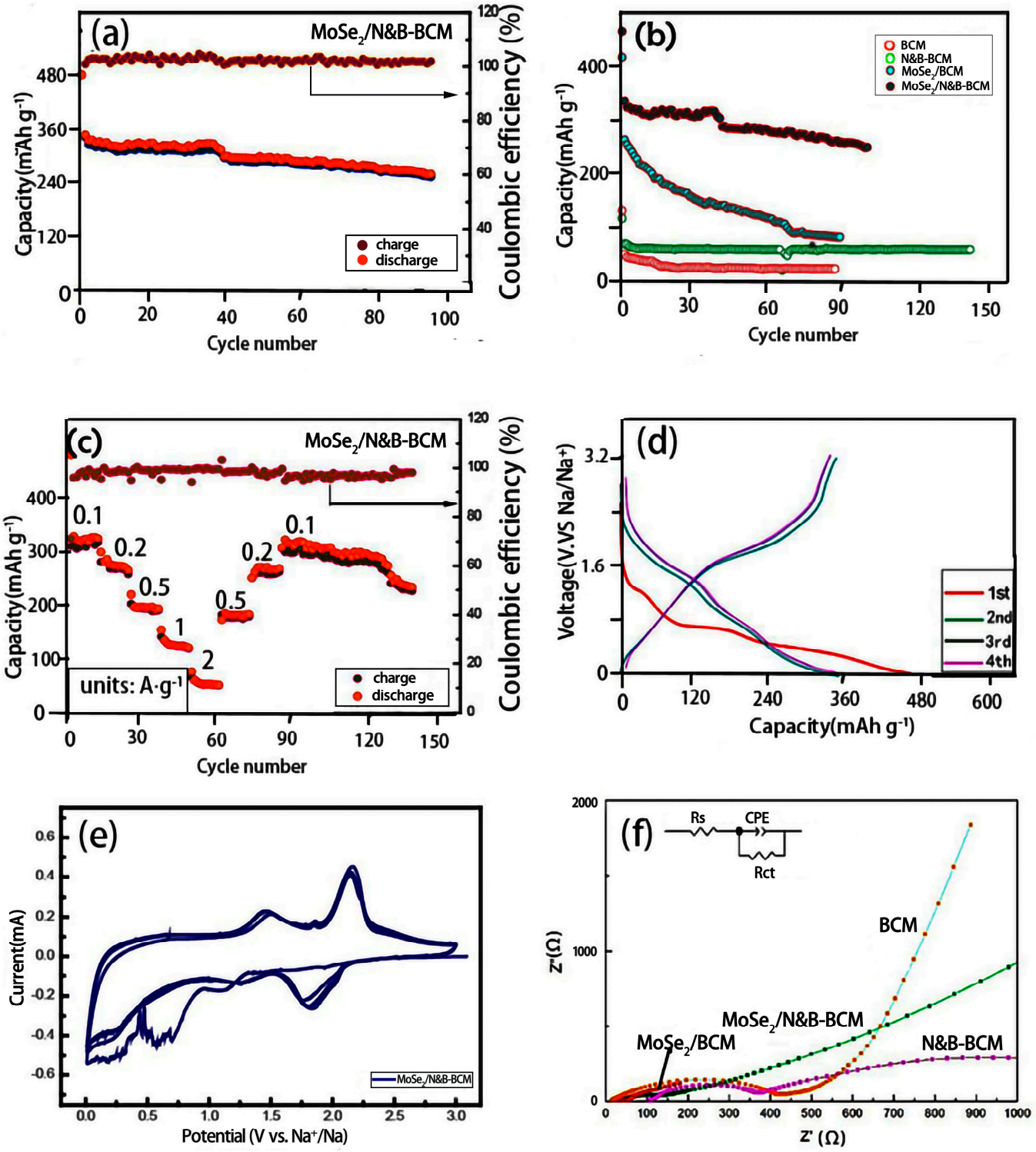


**Figure 5.** (**a**) $MoSe_2$/N&B-BCM cycling performance at 0.5 $A \cdot g^{-1}$. (**b**) BCM, N&B-BCM, $MoSe_2$/BCM, and $MoSe_2$/N&B-BCM materials' cycling performances at 0.5 $A \cdot g^{-1}$. (**c**) Rate performance at different rates from 0.1 to 2 $A \cdot g^{-1}$. (**d**) Galvanostatic charge–discharge profiles at a constant rate of 0.1 $A \cdot g^{-1}$. (**e**) CV curves for $MoSe_2$/N&B-BCM. (**f**) Electrochemical Impedance Spectroscopy of BCM, N&B-BCM, $MoSe_2$/BCM, and $MoSe_2$/N&B-BCM.

**Table 1.** The impedance of BCM, N&B-BCM, MoSe2/BCM, and MoSe2/N&B-BCM with sodium. (Rct: charge migration resistance, Rs: internal resistance).

| Resistance Value | BCM | N&B-BCM | $MoSe_2$/BCM | $MoSe_2$/N&B-BCM |
|---|---|---|---|---|
| Rs | 28.5 Ω | 20.82 Ω | 28.46 Ω | 11.96 Ω |
| Rct | 1719 Ω | 604 Ω | 453 Ω | 182.4 Ω |

Obviously, the diameter of the semicircle related to $MoSe_2$/N&B-BCM is smaller than that of BCM, N&B-BCM, and $MoSe_2$/BCM in a new cell, implying augmented charge transfer efficiency. Meanwhile, the steeper slope of the $MoSe_2$/N&B-BCM electrode also suggests improved ion diffusion, which accords well with the above charge–discharge analysis.

## 4. Conclusions

Compared with the capacity of BCM (98 $mAh{\cdot}g^{-1}$), N&B-BCM (101 $mAh{\cdot}g^{-1}$), and $MoSe_2$/BCM (232 $mAh{\cdot}g^{-1}$), the effects of dual-doped N and B elements with 3D carbon nanofibers on sodium storage properties were systematically studied. $MoSe_2$/N&B-BCM exhibited excellent cyclability in the sodium test (328 $mAh{\cdot}g^{-1}$ after 100 cycles at 0.5 $A{\cdot}g^{-1}$) and rate performance. These outstanding electrochemical performances should be associated with the novel 3D architecture, in which the N and B elements are mainly homogeneously dispersed on the fibers of the BCM. Due to the dual-doped N and B features, $MoSe_2$ complexed with N- and B-doped BCM produces stable composites. Its electronic point actives had already been enhanced, which resulted in stable cyclability and excellent rate performance.

**Author Contributions:** Conceptualization, W.Z.; data curation, W.Z.; formal analysis, W.Z.; investigation, C.L.; methodology, X.Y.; supervision, C.L.; validation, X.Y.; writing—original draft, W.Z. All authors have read and agreed to the published version of the manuscript.

**Funding:** This work was supported by the National Natural Science Foundation of China (NO. 51875384) and the Natural Science Foundation of Shanxi Province (NO. 201801D121085).

**Institutional Review Board Statement:** Not applicable.

**Informed Consent Statement:** Not applicable.

**Data Availability Statement:** Not applicable.

**Conflicts of Interest:** The authors declare no conflict of interest.

## References

1. Wang, Y.; Fu, Q.; Li, C.; Li, H.; Tang, H. Nitrogen and phosphorus dual-doped graphene aerogel confined monodisperse iron phosphide nanodots as an ultrafast and long-term cycling anode material for sodium-ion batteries. *ACS Sustain. Chem. Eng.* **2018**, *6*, 15083–15091. [CrossRef]
2. Slater, M.D.; Kim, D.; Lee, E.; Johnson, C.S. Sodium-ion batteries. *Adv. Funct. Mater.* **2013**, *23*, 947–958. [CrossRef]
3. Qiu, Z.; Zhao, K.; Liu, J.; Xia, S. Nitrogen-doped mesoporous carbon as an anode material for high performance potassium-ion batteries. *Electrochim. Acta* **2020**, *340*, 135947. [CrossRef]
4. Lu, W.; Zhu, J.; He, S.A.; Cui, Z.; Wang, H.; Xu, C.; Liu, Q.; Zou, R. Enhanced reversible sodium storage by thin carbon layer encapsulated MoS2 nanospheres on interwoven carbon nanotubes. *Solid State Ion.* **2021**, *359*, 115522. [CrossRef]
5. Zhao, Y.; Li, X.; Yan, B.; Xiong, D.; Li, D.; Lawes, S.; Sun, X. Recent Developments and Understanding of Novel Mixed Transition-Metal Oxides as Anodes in Lithium-Ion Batteries. *Adv. Energy Mater.* **2016**, *6*, 1502175. [CrossRef]
6. Wu, Y.; Wang, Y.; Shao, S.; Ma, Y.; Zhang, J.; Kang, W.; Xu, J. Transformation of Two-Dimensional Iron Sulfide Nanosheets from FeS2 to FeS as High-Rate Anodes for Pseudocapacitive Sodium Storage. *ACS Appl. Energy Mater.* **2020**, *3*, 12672–12681. [CrossRef]
7. Zhao, W.; Ma, X. Hierarchical Scalelike Yolk–Shell Construction Assembled via Ultrathin $MoSe_2$ Nanoplates Incorporated into Metal–Organic Frameworks Derived Porous Carbon Spheres as Highly Durable Anode for Enhanced Sodium Storage. *ACS Sustain. Chem. Eng.* **2020**, *8*, 19040–19050. [CrossRef]
8. Cheng, L.; Zhang, Y.; Chu, P.; Wang, S.; Li, Y.; Ren, X.; Zhang, P.; Sun, L. Heterostructure enhanced sodium storage performance for $SnS_2$ in hierarchical $SnS_2/Co_3S_4$ nanosheet array composite. *J. Mater. Chem. A* **2021**, *9*, 1630–1642. [CrossRef]
9. Zhao, X.; Zhao, Y.; Huang, B.; Cai, W.; Sui, J.; Yang, Z.; Wang, H.E. $MoSe_2$ Nanoplatelets with Enriched Active Edge Sites for Superior Sodium-ion Storage and Enhanced Alkaline Hydrogen Evolution Activity. *Chem. Eng. J.* **2019**, *382*, 123047. [CrossRef]

10. Hou, H.; Qiu, X.; Wei, W.; Zhang, Y.; Ji, X. Carbon Anode Materials for Advanced Sodium-Ion Batteries. *Adv. Energy Mater.* **2017**, *7*, 1602898. [CrossRef]
11. Lao, M.; Zhang, Y.; Luo, W.; Yan, Q.; Sun, W.; Dou, S.X. Alloy-Based Anode Materials toward Advanced Sodium-Ion Batteries. *Adv. Mater.* **2017**, *29*, 1700622. [CrossRef]
12. Fang, S.; Bresser, D.; Passerini, S. Transition Metal Oxide Anodes for Electrochemical Energy Storage in Lithium- and Sodium-Ion Batteries. *Adv. Energy Mater.* **2019**, *10*, 1902485. [CrossRef]
13. Luo, M.; Yu, H.; Hu, F.; Liu, T.; Cheng, X.; Zheng, R.; Bai, Y.; Shui, M.; Shu, J. Metal Selenides for High Performance Sodium Ion Batteries. *Chem. Eng. J.* **2019**, *380*, 122557. [CrossRef]
14. Niu, F.; Yang, J.; Wang, N.; Zhang, D.; Fan, W.; Yang, J.; Qian, Y. $MoSe_2$-Covered N,P-Doped Carbon Nanosheets as a Long-Life and High-Rate Anode Material for Sodium-Ion Batteries. *Adv. Funct. Mater.* **2017**, *27*, 1700522. [CrossRef]
15. Hwang, J.-Y.; Myung, S.-T.; Sun, Y.-K. Sodium-ion batteries: Present and future. *Chem. Soc. Rev.* **2017**, *46*, 3529–3614. [CrossRef]
16. Wang, J.; Jiang, K.; Shen, B.; Zhen, M. Synergetic Effect of Nitrogen/Sulfur Dual-Doped Hierarchically Porous Carbon Networks for Li–S Batteries. *ACS Sustain. Chem. Eng.* **2019**, *8*, 749–758. [CrossRef]
17. Yabuuchi, N.; Kubota, K.; Dahbi, M.; Komaba, S. Research Development on Sodium-Ion Batteries. *Chem. Rev.* **2014**, *114*, 11636–11682. [CrossRef]
18. Lee, S.J.; Theerthagiri, J.; Nithyadharseni, P.; Arunachalam, P.; Balaji, D.; Kumar, A.M.; Madhavan, J.; Mittal, V.; Choi, M.Y. Heteroatom-doped graphene-based materials for sustainable energy applications: A review. *Renew. Sustain. Energy Rev.* **2021**, *143*, 110849. [CrossRef]
19. Delmas, C. Sodium and sodium-ion batteries: 50 years of research. *Adv. Energy Mater.* **2018**, *8*, 1703137. [CrossRef]
20. Yadav, D.; Amini, F.; Ehrmann, A. Recent advances in carbon nanofibers and their applications—A review. *Eur. Polym. J.* **2020**, *138*, 109963. [CrossRef]
21. Hueso, K.B.; Armand, M.; Rojo, T. High temperature sodium batteries: Status, challenges and future trends. *Energy Environ. Sci.* **2013**, *6*, 734–749. [CrossRef]
22. Ellis, B.L.; Nazar, L.F. Sodium and sodium-ion energy storage batteries. *Curr. Opin. Solid State Mater. Sci.* **2012**, *16*, 168–177. [CrossRef]
23. Chen, J.; Yang, B.; Liu, B.; Lang, J.; Yan, X. Recent advances in anode materials for sodium-and potassium-ion hybrid capacitors. *Curr. Opin. Electrochem.* **2019**, *18*, 1–8. [CrossRef]
24. Wu, Y.; Sun, Y.; Tong, Y.; Liu, X.; Zheng, J.; Han, D.; Li, H.; Niu, L. Recent advances in potassium-ion hybrid capacitors: Electrode materials, storage mechanisms and performance evaluation. *Energy Storage Mater.* **2021**, *41*, 108–132. [CrossRef]
25. Okoshi, T.; Yamada, K.; Hirasawa, T.; Emori, A. Battery condition monitoring (BCM) technologies about lead–acid batteries. *J. Power Sources* **2006**, *158*, 874–878. [CrossRef]
26. Vahid, S.; Abarzadeh, M.; Weise, N.; El-Refaie, A. A Novel Three-Port dc-dc Power Converter with Adaptive Boundary Current Mode Controller for a Residential PV-Battery System. In Proceedings of the 46th Annual Conference of the IEEE Industrial Electronics Society, Singapore, 18–21 October 2020; pp. 4263–4268.
27. Jiang, F.; Yin, L.; Yu, Q.; Zhong, C.; Zhang, J. Bacterial cellulose nanofibrous membrane as thermal stable separator for lithium-ion batteries. *J. Power Sources* **2015**, *279*, 21–27. [CrossRef]
28. Zhou, H.; Lv, P.; Lu, X.; Hou, X.; Zhao, M.; Huang, J.; Xia, X.; Wei, Q. Fibrous network of c@ $MoS_2$ nanocapsule-decorated cotton linters interconnected by bacterial cellulose for lithium-and sodium-ion batteries. *ChemSusChem* **2019**, *12*, 5075–5080. [CrossRef] [PubMed]
29. Zhang, Z.; Zhang, J.; Zhao, X.; Yang, F. Core-sheath structured porous carbon nanofiber composite anode material derived from bacterial cellulose/polypyrrole as an anode for sodium-ion batteries. *Carbon* **2015**, *95*, 552–559. [CrossRef]
30. Ma, L.; Bi, Z.; Xue, Y.; Zhang, W.; Huang, Q.; Zhang, L.; Huang, Y. Bacterial cellulose: An encouraging eco-friendly nano-candidate for energy storage and energy conversion. *J. Mater. Chem. A* **2020**, *8*, 5812–5842. [CrossRef]
31. Foresti, M.L.; Vázquez, A.; Boury, B. Applications of bacterial cellulose as precursor of carbon and composites with metal oxide, metal sulfide and metal nanoparticles: A review of recent advances. *Carbohydr. Polym.* **2017**, *157*, 447–467. [CrossRef]